ELSEVIER

Journal of Power Sources 94 (2001) 40–50

JOURNAL OF POWER SOURCES

www.elsevier.com/locate/jpowsour

Two-phase flow and transport in the air cathode of proton exchange membrane fuel cells

Z.H. Wang[a], C.Y. Wang[a,*], K.S. Chen[b]

[a]*Electrochemical Engine Center, Department of Mechanical and Nuclear Engineering, Pennsylvania State University, University Park, PA 16802, USA*

[b]*Engineering Sciences Center, Sandia National Laboratories, Albuquerque, NM 87185-0834, USA*

Received 29 September 2000; accepted 4 October 2000

Abstract

Two-phase flow and transport of reactants and products in the air cathode of proton exchange membrane (PEM) fuel cells is studied analytically and numerically. Single- and two-phase regimes of water distribution and transport are classified by a threshold current density corresponding to first appearance of liquid water at the membrane/cathode interface. When the cell operates above the threshold current density, liquid water appears and a two-phase zone forms within the porous cathode. A two-phase, multicomponent mixture model in conjunction with a finite-volume-based computational fluid dynamics (CFD) technique is applied to simulate the cathode operation in this regime. The model is able to handle the situation where a single-phase region co-exists with a two-phase zone in the air cathode. For the first time, the polarization curve as well as water and oxygen concentration distributions encompassing both single- and two-phase regimes of the air cathode are presented. Capillary action is found to be the dominant mechanism for water transport inside the two-phase zone of the hydrophilic structure. The liquid water saturation within the cathode is predicted to reach 6.3% at 1.4 A cm^{-2} for dry inlet air.

Keywords: Two-phase transport; PEM fuel cells; Analytical modeling; Numerical simulation; Water management

1. Introduction

Water management is critical for achieving high performance of proton exchange membrane (PEM) fuel cells. As a vessel of protons, the polymer electrolyte membrane requires sufficient water to exhibit a high ionic conductivity. During fuel cell operation, water molecules migrate through the membrane under electro-osmotic drag, fluid convection, and molecular diffusion, making it difficult to retain a high water content within the membrane. Generally, humidification is applied to the inlets of the anode and/or cathode in order to supply water to the membrane region. On the other hand, water is generated at the cathode/membrane interface due to the electrochemical reaction of H^+/O_2. If the water generated is not removed from the cathode at a sufficient rate, cathode flooding may result and the oxygen gas transport is hindered. Thus, a relatively dry air at the cathode inlet is sometimes helpful to remove excessive water, in particular, for the air cathode of direct methanol PEM fuel cells.

Modeling water transport and distribution in PEM fuel cells has been attempted in recent years. Bernardi [1] analyzed the effects of different operating conditions on the water balance in fuel cells. Wang and Savinell [2] included the electrode structure effects on water transport in the catalyst layer. With a pseudo two-dimensional membrane–electrode model, Fuller and Newman [3] simulated a PEM fuel cell operation under the condition of moist gas in electrodes. They obtained the water distribution in the membrane and the net water flux across it. Nguyen and White [4] compared three humidification designs using a combined heat and mass transfer model. Springer et al. [5] predicted the net water-per-proton flux ratio across the membrane. In a later work, Springer et al. [6] fitted their predicted results to the experimental data by assuming that the presence of liquid water only modifies the effective porosity for oxygen gas transport. Bernardi and Verbrugge [7,8] formulated a simplified one-dimensional model for liquid water transport in porous electrodes assuming a constant liquid volume fraction and no interactions between liquid and gas flows.

Recently, Gurau et al. [9] applied a comprehensive model of fluid dynamics and species transport to a full PEM fuel

* Corresponding author. Tel.: +1-814-863-4762; fax: +1-814-863-4848.
E-mail address: cxw31@psu.edu (C.Y. Wang).

0378-7753/01/$ – see front matter
PII: S0378-7753(00)00662-5

Nomenclature

C	species mass concentration (kg kg^{-1})
D	diffusivity (cm^2 s^{-1})
F	Faraday constant (96,487 C mol^{-1})
$\boldsymbol{g}$	gravitational acceleration (cm s^{-2})
h_m	mass transfer coefficient between porous cathode and gas channel (cm s^{-1})
H	total height of cathode and channel (cm)
H_c	cathode thickness ($H_c = H - H_{gc}$) (cm)
H_{gc}	gas channel height (cm)
I	current density (A cm^{-2})
I_{cr}	critical current density (A cm^{-2})
I_0	exchange current density (A cm^{-2})
j	mass flux in y-direction (kg cm^{-2} s^{-1})
$\boldsymbol{j}$	mass flux vector (kg cm^{-2} s^{-1})
k_{rg}	relative permeability of gas phase
k_{rl}	relative permeability of liquid phase
K	permeability of porous cathode (cm^{-2})
L	cathode length (cm)
M	molecular weight (kg mol^{-1})
p	pressure (Pa)
p_c	capillary pressure (Pa)
R	gas constant (J mol^{-1} K^{-1})
RH	relative humidity
s	liquid water saturation
Sh	Sherwood number ($h_m H_{gc}/D$)
t	time (s)
T	temperature (°C)
u	intrinsic velocity in x-direction (cm s^{-1})
$\boldsymbol{u}$	intrinsic velocity vector (cm s^{-1})
v	intrinsic velocity in y-direction (cm s^{-1})
$V_{cathode}$	cathode potential versus SHE (V)
V_{ocp}	open circuit potential versus SHE (V)
x	coordinate (cm)
y	coordinate (cm)

Greek letters

α	net water transport coefficient per proton
α_c	cathodic transfer coefficient
ε	porosity of gas diffusion cathode
η	overpotential (V)
μ	viscosity (kg cm^{-1} s^{-1})
ν	kinetic viscosity (cm^2 s^{-1})
θ_c	contact angle (°)
ρ	density (kg cm^{-3})
ρ_k	kinetic density (kg cm^{-3})
σ	surface tension (N cm^{-1})

Superscripts

H_2O	water
O_2	oxygen
$-$	average value in gas channel

Subscripts

flow	flow channel
g	gas phase
in	inlet
l	liquid phase
ref	reference value
sat	saturated water vapor

cell. Similarly, Yi and Nguyen [10] analyzed two-dimensional hydrodynamics and multicomponent transport in an interdigitated cathode. It should be noted that these recent models are valid only in the absence of liquid water, and they do not account for water condensation and evaporation phase change within porous electrodes.

The importance of two-phase transport in PEM fuel cells has been repeatedly stressed in the literature [5,6]. During fuel cell operation, especially at high current densities, liquid water is likely to appear in the cathode, resulting in two-phase transport phenomena. The transport processes then become significantly more complicated due to the coupled flow of liquid water and gaseous reactants in porous media [11,12]. Liquid water transport by capillary action, dynamic interaction between single- and two-phase zones via evaporation and condensation, and effects of the phase distribution on gas transport remain to be explored.

The present paper describes a numerical study of gas–liquid, two-phase flow and transport in the air cathode of PEM fuel cells including hydrogen and direct methanol fuel cells. In the following section, single- and two-phase transport regimes are first defined and discussed analytically, which is followed by an accurate numerical model based on the multiphase mixture model previously developed by Wang and Cheng [13] for two-phase flow and multicomponent transport in porous media. Two-dimensional simulations are presented to corroborate the analytical estimate of a threshold current density defining the two transport regimes as well as to study the two-phase hydrodynamics and transport of air and liquid water and its effects on the performance of the PEM fuel cell cathode.

2. Problem statement

Consider a porous cathode adjacent to a flow channel, as shown in Fig. 1. The catalyst layer is simplified as an infinitely thin interface between the membrane and the porous cathode. The oxygen reduction reaction at the membrane/cathode interface consumes oxygen and generates water. Transport of the reactant and product occurs in the porous cathode and flow channel. As the current density (i.e. the water generation rate) increases, water is present first as vapor only but gradually condenses to liquid thus leading to the development of two-phase flow and transport in the air cathode. In the present paper, we define onset of the two-phase operating regime when liquid water first appears in the vicinity of the membrane/cathode

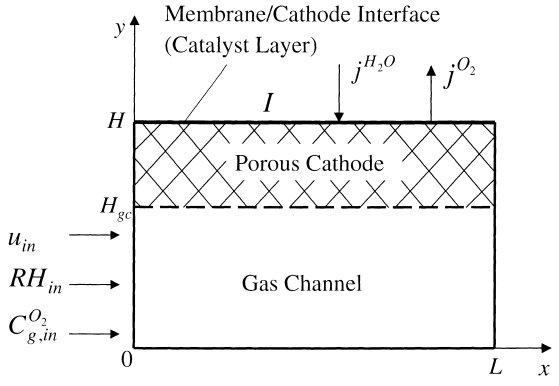

Fig. 1. Schematic of a PEM fuel cell air cathode in simulation.

interface. Correspondingly, a threshold current density can be identified for the boundary between the single- and two-phase transport regimes of the air cathode.

To obtain an analytical estimate of the threshold current density, consider a one-dimensional water transport process along y-direction only. Water generated at the membrane/cathode interface is transported through the cathode into the gas channel and then carried away to the channel exit. Assuming that the net water transport across the membrane to the cathode is quantified by a net water transport coefficient, the rate of water generation at the membrane/cathode interface can then be expressed, according to Faraday's law, as

$$j^{\mathrm{H_2O}}|_{y=H} = -\frac{M^{\mathrm{H_2O}}(1+2\alpha)}{2F} I \tag{1}$$

where α is the net water transport coefficient across the membrane, i.e. the ratio of the water flux across the membrane from the anode to the proton flux transported. Physically, this water flux is a combined result of electro-osmotic drag, fluid convection, and molecular diffusion.

In the case of no liquid formation, gas diffusion is generally the main mechanism for water transport through the porous cathode, and gas convection is negligible due to the small permeability. The water vapor flux across the cathode can thus be calculated by

$$j_{\mathrm{g}}^{\mathrm{H_2O}}|_{y=H_{\mathrm{gc}}} = -D_{\mathrm{g}}^{\mathrm{H_2O}}\varepsilon \frac{\rho_{\mathrm{g}}^{\mathrm{H_2O}}|_{y=H} - \rho_{\mathrm{g}}^{\mathrm{H_2O}}|_{y=H_{\mathrm{gc}}}}{H - H_{\mathrm{gc}}} \tag{2}$$

where $\rho_{\mathrm{g}}^{\mathrm{H_2O}}|_{y=H}$ represents the water vapor density at the membrane/cathode interface, and $H - H_{\mathrm{gc}}$ the thickness of porous cathode, H_{c}. The water vapor density at the cathode/channel interface, $\rho_{\mathrm{g}}^{\mathrm{H_2O}}|_{y=H_{\mathrm{gc}}}$, depends on the mass exchange process between the porous cathode and gas channel. Using the average water vapor density of the cross-section area in the gas channel, $\overline{\rho_{\mathrm{g,flow}}^{\mathrm{H_2O}}}$, one can express the mass flux of water vapor at the cathode/channel interface as

$$j_{\mathrm{g}}^{\mathrm{H_2O}}|_{y=H_{\mathrm{gc}}} = -h_{\mathrm{m}}\left(\rho_{\mathrm{g}}^{\mathrm{H_2O}}|_{y=H_{\mathrm{gc}}} - \overline{\rho_{\mathrm{g,flow}}^{\mathrm{H_2O}}}\right) \tag{3}$$

where h_{m} is the mass transfer coefficient between the porous cathode and gas channel. Combining Eqs. (2) and (3) results in

$$j_{\mathrm{g}}^{\mathrm{H_2O}}|_{y=H_{\mathrm{gc}}} = -\frac{\rho_{\mathrm{g}}^{\mathrm{H_2O}}|_{y=H} - \overline{\rho_{\mathrm{g,flow}}^{\mathrm{H_2O}}}}{1/h_{\mathrm{m}} + H_{\mathrm{c}}/D_{\mathrm{g}}^{\mathrm{H_2O}}\varepsilon} \tag{4}$$

The two mass transfer resistances in the denominator of Eq. (4) are representative of convection mass exchange between the cathode and channel and diffusion in the cathode respectively. The water removal flux given by Eq. (4) should equal the water generation rate given by Eq. (1) under the steady-state condition.

When the water vapor density at the membrane/cathode interface reaches the saturated value corresponding to the operating temperature, liquid water begins to appear, marking the end of the single-phase regime. Combining Eqs. (1) and (4) thus yields the following expression for the threshold current density:

$$I_{\mathrm{cr}} = \frac{\rho_{\mathrm{g,sat}}^{\mathrm{H_2O}} - \overline{\rho_{\mathrm{g,flow}}^{\mathrm{H_2O}}}}{1/h_{\mathrm{m}} + H_{\mathrm{c}}/D_{\mathrm{g}}^{\mathrm{H_2O}}\varepsilon} \frac{2F}{M^{\mathrm{H_2O}}(1+2\alpha)} \tag{5}$$

Note that the threshold current density given by Eq. (5) is dependent on the average water vapor density of the cross-section area in the gas channel. This parameter increases down the channel due to the continual addition of water vapor from the cathode; namely,

$$\begin{aligned} u_{\mathrm{in}} H_{\mathrm{gc}}\left(\overline{\rho_{\mathrm{g,flow}}^{\mathrm{H_2O}}} - \rho_{\mathrm{g,in}}^{\mathrm{H_2O}}\right) &= \int_0^x \left(-j^{\mathrm{H_2O}}|_{y=H}\right)\mathrm{d}x \\ &= \frac{M^{\mathrm{H_2O}}(1+2\alpha)}{2F} Ix \end{aligned} \tag{6}$$

With Eq. (6), Eq. (5) can now be rewritten as

$$I_{\mathrm{cr}} = \frac{2F}{M^{\mathrm{H_2O}}} \frac{\rho_{\mathrm{g,sat}}^{\mathrm{H_2O}}(1 - \mathrm{RH_{in}})}{1+2\alpha} \left(\frac{L}{H_{\mathrm{gc}}}\frac{1}{u_{\mathrm{in}}} + \frac{1}{h_{\mathrm{m}}} + \frac{H_{\mathrm{c}}}{D_{\mathrm{g}}^{\mathrm{H_2O}}\varepsilon}\right)^{-1} \tag{7}$$

where

$$\mathrm{RH_{in}} = \frac{\rho_{\mathrm{g,in}}^{\mathrm{H_2O}}}{\rho_{\mathrm{g,sat}}^{\mathrm{H_2O}}} \tag{8}$$

is the relative humidity of gas at the inlet. Note that the threshold current density is dependent on the water vapor diffusion resistance in the porous cathode, the mass transfer resistance at the porous cathode/gas channel interface, and the ability of air in the channel to carry away water vapor. It reduces with the increases of inlet relative humidity, channel length, and porous cathode thickness and the decreases of inlet velocity, operating temperature, and channel height.

All parameters required to estimate the threshold current density by Eq. (7) are readily available from the operating conditions except for the net water transport coefficient and the mass transfer coefficient at the interface between the porous cathode and flow channel. The net water transport

Table 1
Property parameters used in numerical simulations

Parameter	Symbol	Value	Reference
Water vapor diffusivity	$D_g^{H_2O}$	0.355 $cm^2\ s^{-1}$	Cussler [15]
Oxygen diffusivity	$D_g^{O_2}$	0.284 $cm^2\ s^{-1}$	Cussler [15]
Porosity of air cathode	ε	0.3	Yi and Nguyen [10]
Net water transport coefficient	α	0.3	Assumed
Permeability of porous cathode	K	$1.0 \times 10^{-7}\ cm^2$	Assumed
Surface tension	σ	6.25 $N\ cm^{-1}$	Incropera and DeWitt [16]
Constant in Tafel equation	$I_0/C_{g,ref}^{O_2}$	0.3125 $A\ cm^{-2}$	Yi and Nguyen [10]
Cathodic transfer coefficient	α_c	2	–
Open circuit potential	V_{ocp}	1.1 V	Yi and Nguyen [10]

coefficient is a combined result of electro-osmotic drag by electric field, fluid convection by pressure difference, and molecular diffusion by species concentration difference in the membrane region, thus its rigorous determination requires a full cell analysis. Some estimate of this parameter has been made by Yi and Nguyen [10] for hydrogen fuel cells.

To estimate the mass transfer coefficient at the cathode/channel interface, consider mass transfer in a fully-developed laminar flow through a parallel-plate channel with a constant mass flux applied at one surface and no-flux at the other. In this situation, the dimensionless mass transfer coefficient defined by Sherwood number is given by [14]

$$Sh = \frac{h_m H_{gc}}{D_g} = 2.693 \tag{9}$$

Although, the fuel-cell flow channel differs slightly from the geometry described above because the cathode/channel interface is permeable, the calculation based on the detailed numerical results to be reported in the following yields a Sherwood number of 2.637 for the present problem. This good agreement with Eq. (9) not only indicates that there is negligibly small flow through the cathode of low permeability, but also confirms that the interfacial mass transfer coefficient can be safely represented by Eq. (9).

Using the properties listed in Table 1 and the operating parameters summarized in Table 2, Fig. 2 illustrates the effect of the air inlet velocity on the threshold current density. It can be seen that the threshold current density approaches an asymptotic value at u_{in} of about 2 $m\ s^{-1}$, implying that the water vapor removal is limited by diffusion through the porous cathode under this condition.

Table 2
Base case and its operating conditions

Parameter	Symbol	Value
Total height of cathode and channel	H	0.12 cm
Channel height	H_{gc}	0.07 cm
Cathode length	L	2cm
Relative humidity at the inlet	RH_{in}	3.43%
Oxygen concentration at the inlet	$C_{g,in}^{O_2}$	0.21
Air velocity at the inlet	u_{in}	30cm s^{-1}
Operating pressure	p	1atm
Operating temperature	T	80°C
Cathode overpotential	η	−0.3473 V

While the above approximate analysis and classification yield simple quantification of the two regimes of water transport and distribution in the air cathode, accurate modeling of the two-phase flow and transport must be performed numerically as is shown in Section 3.

3. Numerical modeling

Several prior models have treated the single-phase operation of the air cathode [9,10,17]. The two-phase regime involving two-phase flow and transport in the air cathode has yet to be modeled. Moreover, no model has been able to include both the single- and two-phase regimes as well as their transition. Therefore, the main objective of this section is to present a unified model that encompasses both the single- and two-phase regimes, and ensures a smooth

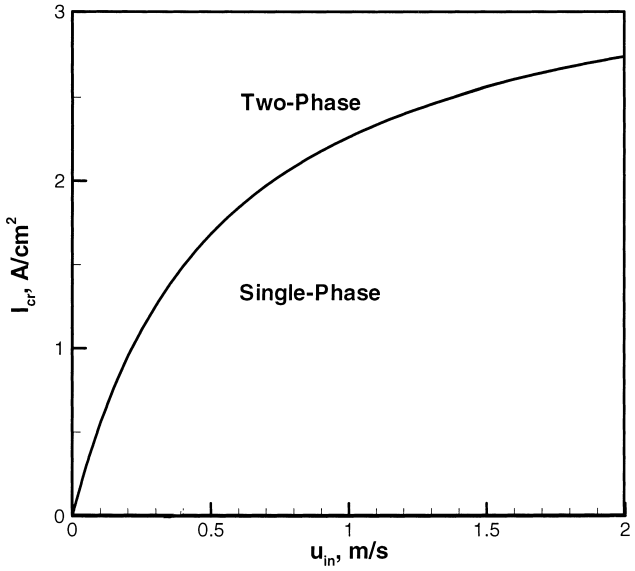

Fig. 2. Effect of the air inlet velocity on the threshold current density defining the boundary between the single- and two-phase regimes.

transition between the two. To account for liquid phase transport by capillary action in the two-phase zone, evaporation–condensation phase change at the evaporation front, and multicomponent gas transport due to both diffusion and convection within the single-phase region, the multiphase mixture model previously developed by Wang and co-workers [13,18–22] is conveniently applied. The reader is referred to Wang and Cheng [13] for details of the multiphase mixture model and its applications to a number of multiphase transport problems in porous media. In the following, only the model assumptions and governing equations for the present problem are summarized.

3.1. Model assumptions

A real gas-diffusion electrode has an extremely complex geometric structure, featuring both micro- and macro-pores as well as a distribution of pore sizes. In addition, the liquid water distribution and the effective surface tension of the gas–liquid interface within a solid matrix depend on hydrophobic or hydrophilic nature of the electrode. As a first step towards modeling the two-phase distribution and transport in air cathodes, it is necessary to invoke simplifying assumptions that are commonly made in the current literature. These are as follows.

1. The gas diffusion electrode is isotropic and homogeneous, and characterized by an effective porosity and permeability.
2. The catalyst layer is treated as an infinitely thin surface of reaction.
3. The cell temperature remains constant.
4. The gas phase is an ideal mixture.

In future work, efforts will be made to incorporate more realistic characteristics of the air cathode structure into the present model framework.

3.2. Governing equations

Continuity

$$\frac{\partial(\varepsilon\rho)}{\partial t} + \nabla\cdot(\varepsilon\rho\boldsymbol{u}) = 0 \tag{10}$$

Momentum conservation

$$\frac{\partial(\varepsilon\rho\boldsymbol{u})}{\partial t} + \nabla\cdot(\varepsilon\rho\boldsymbol{u}\boldsymbol{u}) = \nabla\cdot(\varepsilon\mu\nabla\boldsymbol{u}) - \varepsilon\nabla p + \varepsilon\rho_{\mathrm{k}}\boldsymbol{g} - \varepsilon^2\frac{\mu}{K}\boldsymbol{u} \tag{11}$$

Species conservation

$$\begin{aligned}\frac{\partial}{\partial t}(\varepsilon\rho C) + \nabla\cdot(\varepsilon\gamma_{\mathrm{c}}\rho\boldsymbol{u}C) &= \nabla\cdot(\varepsilon\rho D\nabla C) + \nabla\cdot\{\varepsilon[\rho_{\mathrm{l}}sD_{\mathrm{l}}\nabla C_{\mathrm{l}} \\ &\quad + \rho_{\mathrm{g}}(1-s)D_{\mathrm{g}}\nabla C_{\mathrm{g}} - \rho D\nabla C]\} - \nabla\cdot[(C_{\mathrm{l}} - C_{\mathrm{g}})\boldsymbol{j}_{\mathrm{l}}]\end{aligned} \tag{12}$$

Here, the momentum balance equation has been modified to be valid in both the porous cathode and the open flow channel, reducing to the extended Darcy's law for two-phase flow in porous media with a small permeability and the Navier–Stokes equation inside the flow channel with the porosity being unity and the permeability being infiniteness. Note that $\boldsymbol{u}$ is the intrinsic velocity vector based on the open pore area only. The species transport equation is applicable to oxygen (O_2) as well as water (H_2O). Also, the species concentration on the mass basis has been used instead of the partial density employed in the foregoing order-of-magnitude analysis. They are related by

$$C_j^i = \frac{\rho_j^i}{\rho_j} \tag{13}$$

$$C^i = \frac{\rho^i}{\rho} \tag{14}$$

where superscript i represents a species of O_2 or H_2O, and subscript j a gas (g) or liquid (l) phase.

A unique feature of the multiphase mixture model is that it does not need to track phase interfaces separating single- from two-phase regions, and hence greatly simplifies numerical simulation of the present problem. In fact, all the above governing equations identically reduce to their single-phase counterparts in the limits of the liquid saturation, s, equal to zero and unity, respectively.

3.3. Mixture parameters

In the governing Eqs. (10)–(12), the mixture variables and properties are defined as

Density : $$\rho = \rho_{\mathrm{l}}s + \rho_{\mathrm{g}}(1-s) \tag{15}$$

Concentration : $$\rho C = \rho_{\mathrm{l}}C_{\mathrm{l}}s + \rho_{\mathrm{g}}C_{\mathrm{g}}(1-s) \tag{16}$$

Velocity : $$\rho\boldsymbol{u} = \rho_{\mathrm{l}}\boldsymbol{u}_{\mathrm{l}} + \rho_{\mathrm{g}}\boldsymbol{u}_{\mathrm{g}} \tag{17}$$

Kinetic density : $$\rho_{\mathrm{k}} = \rho_{\mathrm{l}}\lambda_{\mathrm{l}}(s) + \rho_{\mathrm{g}}\lambda_{\mathrm{g}}(s) \tag{18}$$

Viscosity : $$\mu = \frac{\rho_{\mathrm{l}}s + \rho_{\mathrm{g}}(1-s)}{(k_{\mathrm{rl}}/\nu_{\mathrm{l}}) + (k_{\mathrm{rg}}/\nu_{\mathrm{g}})} \tag{19}$$

Diffusion coefficient : $$\rho D = \rho_{\mathrm{l}}sD_{\mathrm{l}} + \rho_{\mathrm{g}}(1-s)D_{\mathrm{g}} \tag{20}$$

Advection correction factor : $$\gamma_{\mathrm{c}} = \frac{\rho(\lambda_{\mathrm{l}}C_{\mathrm{l}} + \lambda_{\mathrm{g}}C_{\mathrm{g}})}{\rho_{\mathrm{l}}sC_{\mathrm{l}} + \rho_{\mathrm{g}}(1-s)C_{\mathrm{g}}} \tag{21}$$

Relative mobilities : $$\lambda_{\mathrm{l}}(s) = \frac{k_{\mathrm{rl}}/\nu_{\mathrm{l}}}{k_{\mathrm{rl}}/\nu_{\mathrm{l}} + k_{\mathrm{rg}}/\nu_{\mathrm{g}}}, \quad \lambda_{\mathrm{g}}(s) = 1 - \lambda_{\mathrm{l}}(s) \tag{22}$$

In addition to the above conservation equations, the multiphase mixture formulation embodies the following important relation for calculating the individual phase velocities

from the mixture flow field:

$$\boldsymbol{j}_{\mathrm{l}} = \frac{\lambda_{\mathrm{l}}\lambda_{\mathrm{g}}K}{v}[\nabla p_{\mathrm{c}} + (\rho_{\mathrm{l}} - \rho_{\mathrm{g}})\boldsymbol{g}] \tag{23}$$

Physically, the first term on RHS represents the capillary flow due to the gradient in meniscus curvature, whereas the second term accounts for gravity-induced phase migration. The individual phase velocities (i.e. intrinsic velocities based on the open pore area rather than phase-occupied areas) are then calculated from

$$\varepsilon\rho_{\mathrm{l}}\boldsymbol{u}_{\mathrm{l}} = \boldsymbol{j}_{\mathrm{l}} + \lambda_{\mathrm{l}}\varepsilon\rho\boldsymbol{u} \tag{24}$$

$$\varepsilon\rho_{\mathrm{g}}\boldsymbol{u}_{\mathrm{g}} = -\boldsymbol{j}_{\mathrm{l}} + \lambda_{\mathrm{g}}\varepsilon\rho\boldsymbol{u} \tag{25}$$

3.4. Constitutive relations

As a first approximation, the gas-diffusion electrode is treated as a homogeneous porous medium with the relative permeabilities for liquid and gas phases represented by [18]

$$k_{\mathrm{rl}} = s^3 \quad \text{and} \quad k_{\mathrm{rg}} = (1-s)^3 \tag{26}$$

Similarly, the capillary pressure between the two phases can be expressed as [13]

$$p_{\mathrm{c}} = \sigma\cos\theta_{\mathrm{c}}\left(\frac{\varepsilon}{K}\right)^{1/2}[1.417(1-s) - 2.120(1-s)^2 + 1.263(1-s)^3] \tag{27}$$

where σ is the surface tension at the gas–liquid interface, and θ_{c} the contact angle. The surface tension is taken to be $0.0625\ \mathrm{N\ m^{-1}}$ for the liquid water–air system at 80°C, whereas θ_{c} is dependent upon the hydrophilic (i.e. $0^\circ \le \theta_{\mathrm{c}} < 90^\circ$) or hydrophobic (i.e. $90^\circ \le \theta_{\mathrm{c}} \le 180^\circ$) nature of the gas-diffusion layer, and thus varies with the Teflon content. In the present work, θ_{c} is chosen to be zero to simulate a hydrophilic electrode. A parametric study by varying θ_{c} will be conducted in a separate publication to access important effects of the wetting property of air cathodes on two-phase transport and distribution.

3.5. Equilibrium conditions

In the present study, liquid water is considered to appear in the porous cathode only when the water vapor pressure reaches its saturated value at the operating temperature. Inside the two-phase zone, thermodynamic equilibrium is assumed to hold true, and thus the concentrations of water in gas and liquid phases given by their equilibrium values, respectively, are

$$C^{\mathrm{H_2O}}_{\mathrm{g,sat}} = \frac{M^{\mathrm{H_2O}}p_{\mathrm{v}}(T)}{R\rho_{\mathrm{g}}T} \quad \text{and} \quad C^{\mathrm{H_2O}}_{\mathrm{l,sat}} = 1 \tag{28}$$

where $p_{\mathrm{v}}(T)$ is the water vapor saturation pressure, and can be obtained from the steam table. Thus, the liquid saturation, s, can be determined from the mixture concentration of water, C, via the following relation:

$$s = \frac{\rho_{\mathrm{g}}(C^{\mathrm{H_2O}} - C^{\mathrm{H_2O}}_{\mathrm{g,sat}})}{\rho_{\mathrm{l}}(C^{\mathrm{H_2O}}_{\mathrm{l,sat}} - C^{\mathrm{H_2O}}) + \rho_{\mathrm{g}}(C^{\mathrm{H_2O}} - C^{\mathrm{H_2O}}_{\mathrm{g,sat}})} \tag{29}$$

Similarly, for oxygen

$$C^{\mathrm{O_2}}_{\mathrm{l,sat}} = 0 \quad \text{and} \quad C^{\mathrm{O_2}}_{\mathrm{g,sat}} = \left[\frac{\rho_{\mathrm{l}}s}{\rho_{\mathrm{g}}(1-s)} + 1\right]C^{\mathrm{O_2}} \tag{30}$$

within the two-phase zone, assuming that oxygen is insoluble in the liquid phase.

3.6. Boundary conditions

At the inlet of the gas channel, constant flow rate and mass concentration of each species are specified. At the outlet, both velocity and concentration fields are assumed to be fully developed. Hence, at $0 < y < H_{\mathrm{gc}}$

$$u|_{x=0} = u_{\mathrm{in}}, \qquad v|_{x=0} = 0, \qquad C^{\mathrm{H_2O}}|_{x=0} = \frac{\rho^{\mathrm{H_2O}}_{\mathrm{g,sat}}\mathrm{RH}_{\mathrm{in}}}{\rho_{\mathrm{g}}}, \quad C^{\mathrm{O_2}}|_{x=0} = C^{\mathrm{O_2}}_{\mathrm{in}} \tag{31}$$

$$\left.\frac{\partial u}{\partial x}\right|_{x=L} = 0, \qquad v|_{x=L} = 0, \qquad \left.\frac{\partial C^{\mathrm{H_2O}}}{\partial x}\right|_{x=L} = 0, \quad \left.\frac{\partial C^{\mathrm{O_2}}}{\partial x}\right|_{x=L} = 0 \tag{32}$$

at $H_{\mathrm{gc}} \le y \le H$

$$u|_{x=0} = 0, \qquad v|_{x=0} = 0, \qquad \left.\frac{\partial C^{\mathrm{H_2O}}}{\partial x}\right|_{x=0} = 0, \quad \left.\frac{\partial C^{\mathrm{O_2}}}{\partial x}\right|_{x=0} = 0 \tag{33}$$

$$u|_{x=L} = 0, \qquad v|_{x=L} = 0, \qquad \left.\frac{\partial C^{\mathrm{H_2O}}}{\partial x}\right|_{x=L} = 0, \quad \left.\frac{\partial C^{\mathrm{O_2}}}{\partial x}\right|_{x=L} = 0 \tag{34}$$

At the membrane/cathode interface where the oxygen reduction reaction occurs

$$u|_{y=H} = 0, \qquad \varepsilon v|_{y=H} = \frac{(j^{\mathrm{O_2}} + j^{\mathrm{H_2O}})|_{y=H}}{\rho|_{y=H}} \tag{35}$$

and

$$\left[\gamma_{\mathrm{c}}\rho\varepsilon v C - \Gamma\frac{\partial(\rho C)}{\partial y} + (C_{\mathrm{l,sat}} - C_{\mathrm{g,sat}})\frac{\lambda_{\mathrm{l}}\lambda_{\mathrm{g}}K}{v}(\rho_{\mathrm{l}} - \rho_{\mathrm{g}})g\right]\Bigg|_{y=H} = j|_{y=H} \tag{36}$$

for both species O_2 and H_2O. Eq. (36) was derived by Cheng and Wang [22] to include three diffusion mechanisms in a compact form: mass diffusion through liquid and gas phases,

respectively, and capillary diffusion within the two-phase zone. The effective diffusivity, Γ, in Eq. (36) is thus defined as

$$\Gamma = \varepsilon D_{\mathrm{g}} \text{ in all gas regions,}$$
$$\Gamma = \frac{(C_{\mathrm{l,sat}} - C_{\mathrm{g,sat}})\rho_{\mathrm{l}} D_{\mathrm{c}}}{\rho_{\mathrm{l}} C_{\mathrm{l,sat}} - \rho_{\mathrm{g}} C_{\mathrm{g,sat}}} \text{ in the two-phase region} \quad (37)$$

where the capillary diffusion coefficient, D_{c}, is given by

$$D_{\mathrm{c}} = \frac{\lambda_{\mathrm{l}}\lambda_{\mathrm{g}} K}{v}\left(-\frac{\mathrm{d}p_{\mathrm{c}}}{\mathrm{d}s}\right) \quad (38)$$

The O_2 mass flux at this boundary can be expressed as

$$j^{\mathrm{O_2}}|_{y=H} = \frac{M^{\mathrm{O_2}}}{4F} I \quad (39)$$

whereas the H_2O mass flux has been given by Eq. (1). Tafel equation is employed to describe the local current density along the membrane/cathode interface; namely,

$$I = I_0 \frac{(1-s)C_{\mathrm{g}}^{\mathrm{O_2}}|_{y=H}}{C_{\mathrm{g,ref}}^{\mathrm{O_2}}} \exp\left(-\frac{\alpha_{\mathrm{c}} F}{RT}\eta\right) \quad (40)$$

where the term $(1-s)$ is used to account for the fraction of surface rendered inactive by the presence of liquid water.

At the bottom of the gas channel,

$$u|_{y=0} = 0, \qquad v|_{y=0} = 0, \qquad \left.\frac{\partial C^{\mathrm{H_2O}}}{\partial y}\right|_{y=0} = 0,$$
$$\left.\frac{\partial C^{\mathrm{O_2}}}{\partial y}\right|_{y=0} = 0 \quad (41)$$

3.7. Cathode potential

Based on the reference that the membrane phase potential is zero at the membrane/cathode interface, the cathode potential can then be related to the cathode polarization overpotential by

$$V_{\mathrm{cathode}} = V_{\mathrm{ocp}} + \eta \quad (42)$$

where V_{ocp} is the open circuit potential of the air cathode in reference to the standard hydrogen electrode (SHE). Note that the cell voltage is equal to the cathode potential minus the ohmic potential drop across the membrane and the anode overpotential.

4. Results and discussion

The coupled governing Eqs. (10)–(12) with the boundary Eqs. (31)–(36) and (41) are solved numerically by a finite-volume-based finite difference method. Numerical details were previously given by Wang [18], and thus are not repeated here. The relevant parameters used in all simulations reported in the following are listed in Table 1.

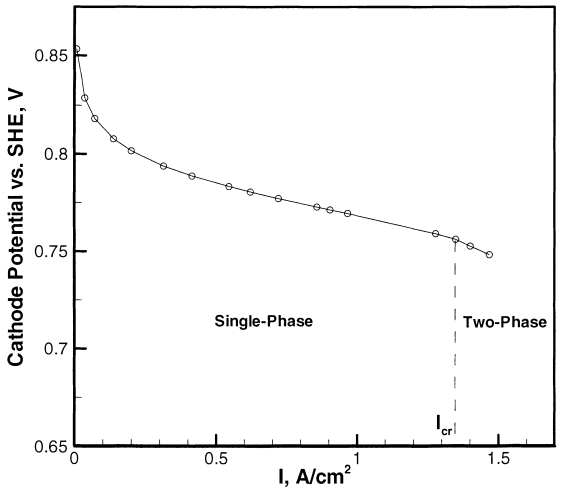

Fig. 3. Polarization curve encompassing both single- and two-phase regimes of the porous cathode.

Fig. 3 shows a simulated cathode polarization curve under the operating conditions described in Table 2. Note that a dry inlet is chosen as a case of study here because of recent interest in PEM fuel cells without external humidification [23] or low-humidity, self-sustaining fuel cells for portable electronics. In addition, the dry inlet of the air cathode is of potential relevance to direct methanol fuel cells [24].

The cathode polarization curve is obtained by varying the surface overpotential with a constant air flow rate at the inlet. This curve only considers the voltage loss at the cathode, and does not include the anode kinetic polarization and membrane ohmic loss. Thus, the polarization curve is higher than experimental results as expected, but its general trend compares well to typical experiments [6]. At low current densities, the cathode activation overpotential is solely responsible for the potential losses of the cathode. At higher current densities, more oxygen is consumed and more water is generated at the membrane/cathode interface due to both the electrochemical reaction and the water transport across the membrane from the anode. The cathode polarization then begins to be limited by the transport of O_2. As the current density exceeds the threshold value, i.e. 1.35 A cm^{-2} in the present case (in comparison, its analytical estimate is 1.26 A cm^{-2} as can be obtained from Fig. 2), more water is produced than that possibly carried away by air from the electrode, and liquid water starts to form in the vicinity of the membrane/cathode interface. The predicted onset of the two-phase regime at 1.35 A cm^{-2} may appear a little high, but this value corresponds to an extremely small cell (i.e. 2 cm long) and the dry inlet air. Both Eq. (7) and numerical calculations indicate that the onset current density for the two-phase regime drops to 0.64 A cm^{-2} for 5 cm long cells with dry air at the inlet.

The presence of liquid water reduces the pore spaces for oxygen transport to the reaction surface as well as renders part of the surface electrochemically inactive. These effects result in a slightly steeper slope of the cathode potential

curve upon the threshold current density, as can be seen from Fig. 3. Clearly, a two-phase model is warranted for fuel cells operated at such high current densities, an operating range of special interest for transportation applications. An advantage of the present two-phase model is that it not only provides a unified formulation for both single-phase analysis at low current densities and two-phase calculation at higher values, but also predicts and ensures the smooth transition from the single- to two-phase region automatically.

With further increase in the cell current density, the two-phase zone expands and its evaporation front propagates towards the cathode/channel interface. The numerical simulation shows that the evaporation front reaches the cathode/channel interface at an average current density of 1.47 A cm^{-2}, beyond which point two-phase flow appears in the cathode channel. This is beyond the scope of the present work.

Fig. 4 shows the velocity field of the two-phase mixture in the cathode and gas channel for the base case (i.e. at the average cell current density of 1.4 A cm^{-2}). As expected, there is a large difference in the velocity scale between the porous region and the open channel. The mixture velocity in the porous cathode is at least two orders of magnitude smaller than that in the open channel, indicating that gas diffusion is the dominant transport mechanism in the single-phase region of the porous cathode. The flow field in the open channel is fully developed in view of the large aspect ratio of the channel length to width (equal to 29 in the present case), as can be seen from Fig. 4 where the channel length is, however, not drawn to scale for better view. The velocity distribution in the conventional flow field such as the one studied in the present work is relatively simple and could be analytically determined; however, a numerical analysis based on the comprehensive model as presented here becomes necessary for complex designs such as the interdigitated flow field [10]. Magnified plots of individual

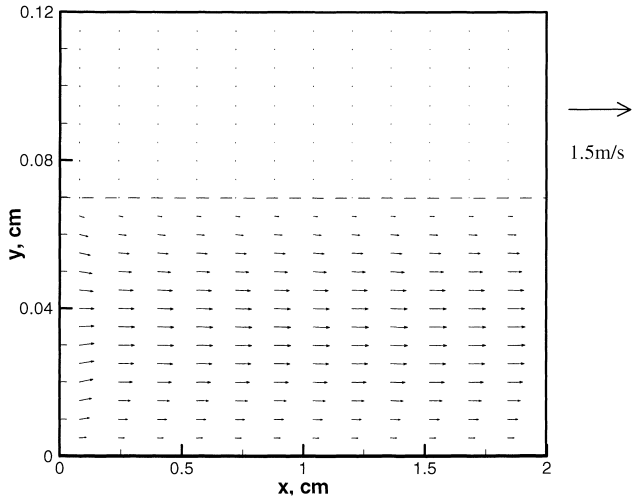

Fig. 4. Two-phase mixture velocity field in the porous cathode and flow channel at the current density of 1.4 A cm^{-2}.

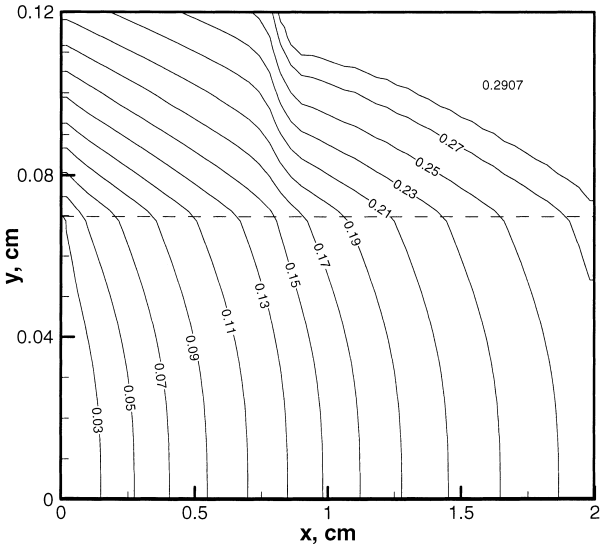

Fig. 5. Water vapor concentration contours in the porous cathode and flow channel at the current density of 1.4 A cm^{-2}.

phase velocity fields within the porous cathode region are presented in Fig. 7(a) and (b) and discussed in detail therein.

Fig. 5 displays the water vapor concentration distribution in the porous cathode and flow channel. As the air flows down the channel, water vapor is continually added from the cathode, resulting in an increased water vapor concentration along the channel. This leads to a decreased concentration gradient in water vapor, and hence a lower water vapor diffusion flux from the membrane/cathode surface to the gas channel. As a result, liquid water may first appear in the vicinity of the membrane/cathode interface near the channel outlet. A two-phase zone at this location is indeed predicted in the present simulation shown in Fig. 5, where the water vapor mass concentration is seen to be kept at the saturated value, i.e. 0.2907, corresponding to the operating temperature of 80°C. It is also seen that the two-phase zone is confined within the cathode at the average current density of 1.4 A cm^{-2}.

Fig. 6 shows the liquid water saturation distribution in the same case. In accordance with Fig. 5, liquid water is seen in the upper-right corner to coexist with the saturated water vapor. The largest liquid amount predicted is around 6.3% at the current density of 1.4 A cm^{-2}. This value is lower than that reported experimentally, likely because the present study simulates a single channel whereas experimental fuel cell fixtures usually use series-connected channels. With the effective channel length extended, a higher liquid saturation may result. Also, a dry inlet is used in the present simulations, whereas many experimental systems humidify the air stream. The numerical results indicate that the mass flux of liquid water due to gravity is less than 0.1% of that caused by capillary action in the two-phase zone. This is because the Bond number [16], defined as $(\rho_l - \rho_g)gH_c^2/\sigma$, is about 0.04, implying the negligible gravity effect as compared with the surface tension effect in the two-phase zone. Thus,

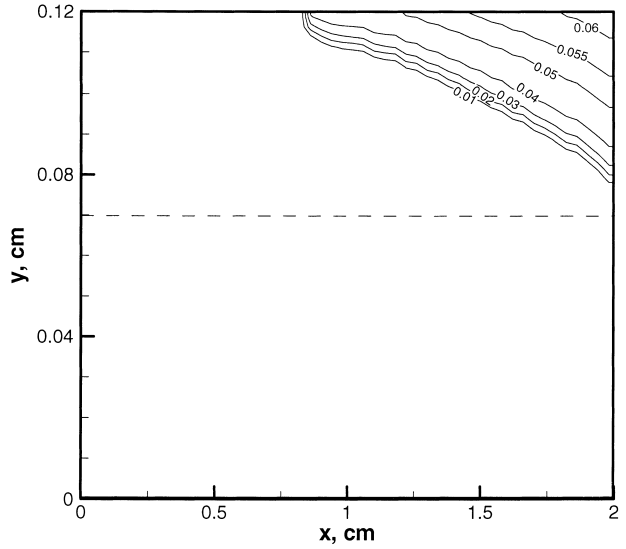

Fig. 6. Liquid water saturation contours in the porous cathode and flow channel at the current density of 1.4 A cm^{-2}. The evaporation front separating the two-phase zone from the single-phase region is approximately represented by the contour of $s = 0.01$.

the liquid water is transported mainly by capillary action to the evaporation front. The front can be approximately depicted by the contour of $s = 0.01$ shown in Fig. 6.

To display individual velocity field of each phase in the porous cathode, the gas and liquid velocities are calculated from the mixture velocity according to Eqs. (24) and (25) and shown in Fig. 7(a) and (b), respectively. Within the two-phase zone, liquid water flows towards the evaporation front under capillary action. The maximum liquid velocity is approximately 2.3×10^{-5} m s^{-1}. The gas velocity field shown in Fig. 7(b) differs from the liquid velocity by three orders of magnitude and displays opposite patterns in the single- and two-phase regions. In the single-phase region, the gas velocity is primarily normal towards the cathode/channel interface due to the non-zero gas velocity created by the electrochemical reaction of H^+/O_2. It is noted from Eq. (35) along with Eqs. (1) and (39) that the normal velocity at the reaction surface is negative (pointing away from it), in accordance with the physical process that hydrogen ions are recombined with O_2 to produce water. Across the evaporation front, however, the gas flow reverses its direction, leaving away from the evaporation front again due to capillary action in the two-phase zone. The maximum gas velocity is approximately 0.005 m s^{-1} in the single-phase region, while 0.02 m s^{-1} in the two-phase zone. For a cathode thickness of 0.0005 m and the gas diffusivity of around 3×10^{-5} m^2 s^{-1} for both water vapor and oxygen, the Peclet number for gas transport is thus 0.08 and 0.32 for single- and two-phase zones, respectively. This implies a

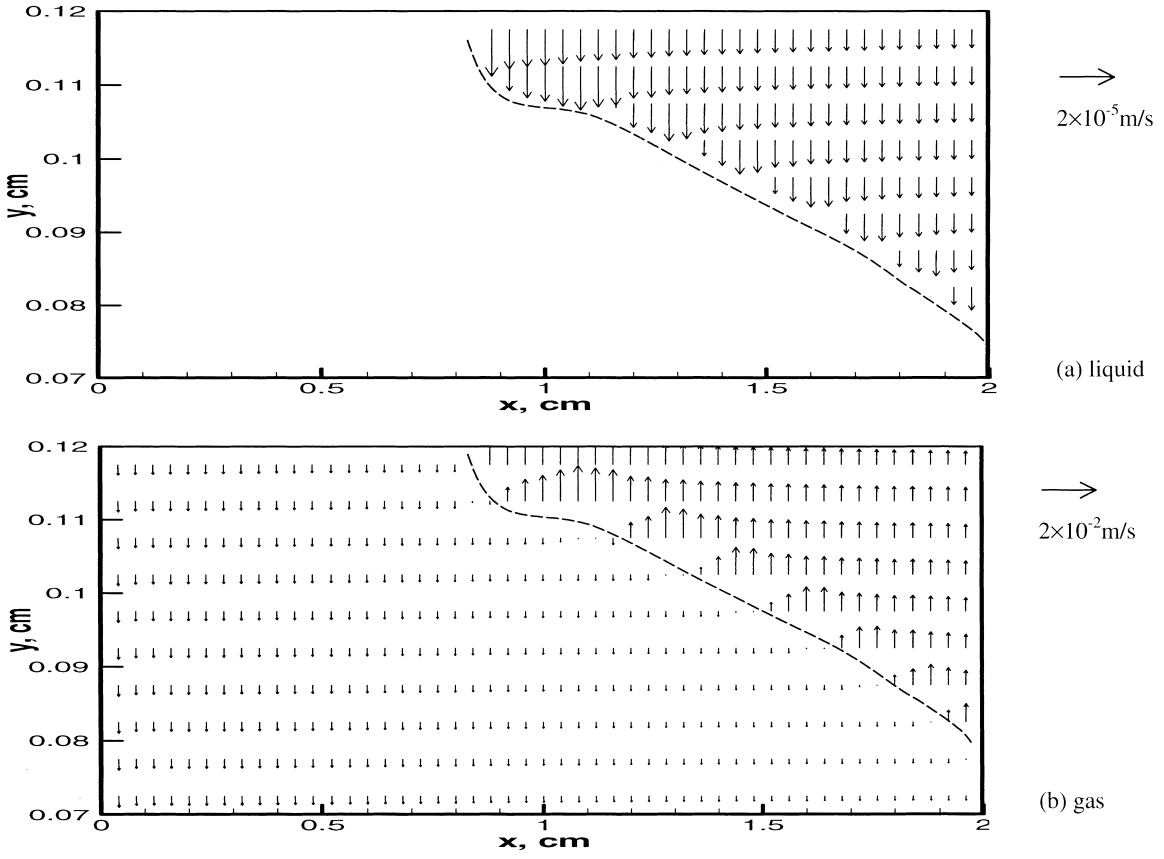

Fig. 7. Liquid and gas velocity fields at the average current density of 1.4 A cm^{-2}: (a) liquid; (b) gas.

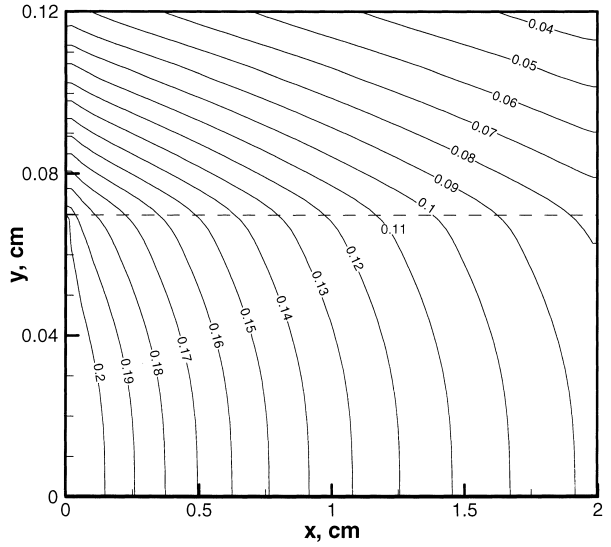

Fig. 8. Oxygen concentration contours in the porous cathode and flow channel at the current density of 1.4 A cm^{-2}.

definitely negligible contribution of gas convection in the single-phase region but some effect of gas convection in the two-phase zone.

Fig. 8 shows the oxygen concentration distribution in both the cathode and open channel at the same current density of 1.4 A cm^{-2}. It can be seen that about 40% of the inlet oxygen has been consumed at the half-length of the channel. At higher current densities, this fraction becomes larger, leaving the channel outlet section nearly depleted of oxygen. A direct consequence of the non-uniform oxygen concentration profile along the reaction surface is the non-uniform current density distribution, because the oxygen reduction reaction is first-order as indicated by Eq. (40). This is shown in Fig. 9, where the local current density is equal to 2.22 A cm^{-2} at the inlet, but only 0.86 A cm^{-2} near the outlet. Thus, the water generated at the inlet is 2.5 times of that at the outlet. A slightly abrupt change in the slope is also noted from Fig. 9 at $x = 0.8$ cm for the local current density profile. This location corresponds exactly to the beginning of the two-phase zone along the reaction surface. The local current density is reduced as liquid water forms, and subsequently impedes the oxygen supply to the electrochemical reaction surface.

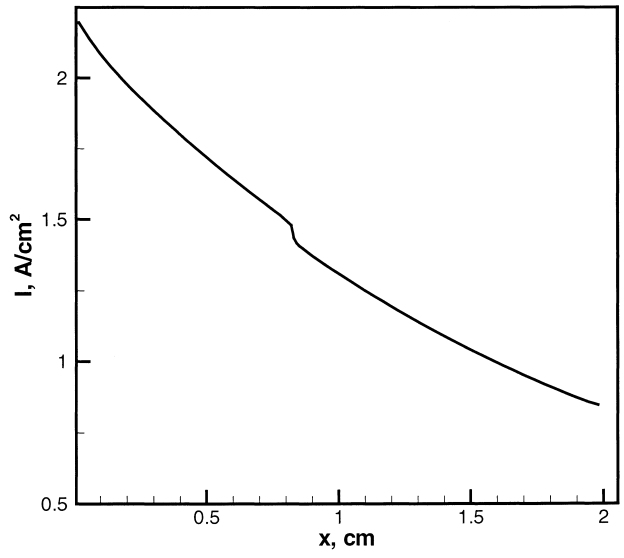

Fig. 9. Local current density distribution at the average of 1.4 A cm^{-2}.

5. Conclusions

Single- and two-phase regimes of water transport and distribution in PEMFC air cathodes have been defined by a threshold current density corresponding to first appearance of liquid water at the membrane/cathode interface. An analytical estimate of the threshold current density was obtained. A two-phase flow and transport model was developed to predict liquid water formation and its effects on the electrochemical kinetics at the membrane/cathode interface and reactant and product transport in the air cathode. The present model is novel in that it encompasses both single- and two-phase regimes corresponding to low and high current densities and therefore is capable of predicting the transition between the two regimes. The water liquid and vapor transport is controlled by capillary action and molecular diffusion, respectively, due to negligible small air velocity within the porous electrode.

The present two-phase model is directly applicable to the air cathode of both hydrogen and direct-methanol fuel cells. In the latter case (DMFC), the two-phase region might be more extensive due to large electro-osmotic and diffusion fluxes of liquid water from the DMFC anode. Similarly, the DMFC anode, where the liquid phase is a methanol aqueous mixture and the gas phase is carbon dioxide, can be treated by the present model.

Future work will include the following activities.

1. Integrate the two-phase cathode model into a multi-dimensional full-cell model (Um et al. [17]) to examine overall cell performance at high current densities. This integration will permit addressing the coupling between the water content and water activity determined by the state of water at the membrane/cathode interface. In other words, the liquid water formation within the cathode may in turn impact the water transport within the membrane and hence its ionic conductivity and ohmic potential drop.
2. Use the two-phase model to properly assess the beneficial effects of an interdigitated flow field design on cell performance in the high current density regime.
3. Perform quantitative comparisons between the numerical predictions and localized experimental measurements.
4. Extend the two-phase model to more accurately incorporate wetting characteristics of the gas-diffusion

electrode and hence assess their effects on cell performance at high current densities.

Acknowledgements

This work was partially supported by Sandia National Laboratories. Sandia is a multiprogram laboratory operated by Sandia Corporation, a Lockheed Martin Company, for the United States Department of Energy under Contract DE-AC04-94AL85000. The work is also supported by NSF under Grant no. DUE-9979579.

References

[1] D.M. Bernardi, J. Electrochem. Soc. 137 (1990) 3344.
[2] J.T. Wang, R.F. Savinell, Electrochim. Acta 37 (1992) 2737.
[3] T.F. Fuller, J. Newman, J. Electrochem. Soc. 140 (1993) 1218.
[4] T.V. Nguyen, R.E. White, J. Electrochem. Soc. 140 (1993) 2178.
[5] T.E. Springer, T.A. Zawodzinski, S. Gottesfeld, J. Electrochem. Soc. 138 (1991) 2334.
[6] T.E. Springer, M.S. Wilson, S. Gottesfeld, J. Electrochem. Soc. 140 (1993) 3513.
[7] D.M. Bernardi, M.W. Verbrugge, AIChE J. 37 (1991) 1151.
[8] D.M. Bernardi, M.W. Verbrugge, J. Electrochem. Soc. 139 (1992) 2477.
[9] V. Gurau, H. Liu, S. Kakac, AIChE J. 44 (1998) 2410.
[10] J.S. Yi, T.V. Nguyen, J. Electrochem. Soc. 146 (1999) 38.
[11] A.E. Scheidegger, The Physics of Flow Through Porous Media, University of Toronto Press, Toronto, 1958.
[12] J. Bear, Dynamics of Fluids in Porous Media, Elsevier, New York, 1972.
[13] C.Y. Wang, P. Cheng, Adv. Heat Transfer 30 (1997) 93.
[14] W.M. Kays, M.E. Crawford, Convective Heat and Mass Transfer, McGraw-Hill, New York, 1993.
[15] E.L. Cussler, Diffusion: Mass Transfer in Fluid Systems, Cambridge University Press, New York, 1984.
[16] F.D. Incropera, D.P. DeWitt, Fundamentals of Heat and Mass Transfer, Wiley, New York, 1985.
[17] S. Um, C.Y. Wang, K.S. Chen, Computational fluid dynamics modeling of proton exchange membrane fuel cells, J. Electrochem. Soc. 147 (2000) 4485.
[18] C.Y. Wang, Numerical Heat Transfer B, Fundam. 31 (1997) 85.
[19] C.Y. Wang, C. Beckermann, Int. J. Heat Mass Transfer 36 (1993) 2747.
[20] C.Y. Wang, P. Cheng, Int. J. Heat Mass Transfer 39 (1996) 3607.
[21] C.Y. Wang, in: D.B. Ingham, I. Pop (Eds.), Transport Phenomena in Porous Media, Elsevier, 1998, pp. 383–396.
[22] P. Cheng, C.Y. Wang, Int. J. Heat Mass Transfer 39 (1996) 3619.
[23] F.N. Buchi, S. Srinivasan, J. Electrochem. Soc. 144 (1997) 2767.
[24] L. Liu, C. Pu, R. Viswanathan, Q. Fan, R. Liu, E.S. Smotkin, Electrochim. Acta 43 (1998) 3657.